Journal of Photochemistry & Photobiology, A: Chemistry 460 (2025) 116160

Contents lists available at ScienceDirect

Journal of Photochemistry & Photobiology, A: Chemistry

journal homepage: www.elsevier.com/locate/jphotochem

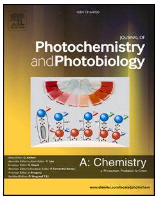

Green synthesis of infrared controlled AgNP/graphite/polyvinylidene fluoride composite membranes for removal of organic pollutants

Huseyin Gumus [1]

Osmaneli Vocational School, Bilecik Seyh Edebali University, 11500 Osmaneli, Bilecik, Turkey

ARTICLE INFO

Keywords:
Fouling resistance
Green synthesis
Quince seed extract
PVDF
Silver particle

ABSTRACT

The effectiveness of light-sensitive particle-added composites as alternative materials in the treatment of waste water was investigated. Infrared responsive polyvinylidene membranes were prepared with anchoring the graphite supported silver particles reduced by quince seed extract. X-ray diffractometer, scanning electron microscope and Fourier transform infrared spectroscopy analysis were used to characterize physicochemical and structural properties of composites. Photoluminescence, surface area and contact angle measurements were carried out. The filtration performances of the membranes were tested under infrared light in a continuous flow system. Methyl orange and bovine serum albumin solutions were used as model pollutants. The silver-graphite additive acted as light absorber and energy converter. Owing to the photothermal effect, the water flux, rejection and roughness of the AgNP-G-P membrane improved significantly, and those were recorded as 74.7 $L.m^{-2}.h^{-1}.bar^{-1}$, 54.6 % and, 75.0, respectively (32.5, 22 and 74.1 %, respectively, for PVDF). The composites almost retained their initial performance after repeated use and did not cause solution leaching. In this study photothermal particles, which are frequently used in medical applications, were successfully adapted to the filtration system. It has the ability to add a specific and new dimension to the protection of the environment by purifying wastewater.

1. Introduction

Compared with ceramic membranes, polymeric membranes have attracted great attention from researchers and industrial users due to their easier to prepare. Their controllability during the preparation phase, and practical application in gas separation, fuel cells, bioreactors and water purification are main reasons for this preference [1,2]. PVDF's high physical and chemical resistance, easy processability and ultraviolet–visible radiation resistance compared to other polymers have made it the privileged membrane material. The biggest disadvantage encountered in PVDF, which are widely used as ultra, micro and nano filtration membranes, is the fouling that occurs on the membrane surface. Its hydrophobic structure promotes the rapid accumulation of organic molecules, microorganisms, proteins and dyes [3,4]. The fouling, which causes a decrease in water flux and rejection performance, can be partially eliminated by chemical washing. However, this method causes a decrease in membrane durability and an increase in filtration costs [5]. In the solution phase of membrane preparation, fouling is attempted to be prevented by adding combinations such as Al_2O_3, FeO, TiO_2, graphene derivatives, Ag and Ag-metal oxide, as well as organic additives such as PVA, PEG, cellulose and chitosan (i) or by grafting antimicrobial and hydrophilic structures onto the membrane surface (ii) [6,7]. Another important effect that increases filtration efficiency and membrane life by reducing fouling is the photocatalytic degradation of impurities. Semiconductor additives such as TiO_2, ZnO, WO_3 and Ag_3PO_4 are effective in both regulating the physical structure of the membrane and gaining light sensitivity of the membrane for photocatalysis [8].

However, in addition to their wide band-gap energies of mentioned semiconductors, low sensitivity and fast electron/hole recombination rates of them with the structural wear on the material surface due to ultraviolet light sensitivity create a drawback. Research has been carried out to shift the photo-induce in the UV region to the visible region by doping at surface sites or creating defects in the crystal lattice [9,10]. With the addition of 0.1 % Sm to TiO_2, which is frequently used due to its low cost, high photocatalytic activity and optical-electronic properties, the band gap energy value decreased to 2.673 eV and was effective in the photocatalytic degradation of 99 % methylene blue [4]. Graphite,

---

E-mail address: huseyin.gumus@bilecik.edu.tr.

[1] ORCID No: 0000-0002-2029-7978.

https://doi.org/10.1016/j.jphotochem.2024.116160
Received 21 August 2024; Received in revised form 27 October 2024; Accepted 12 November 2024

graphene oxide (GO), and reduced graphene oxide (rGO) with graphene quantum dots were combined with semiconductors and used to obtain photocatalytic membranes. Thus, the membrane's roughness, mechanical-chemical resistance, electronegativity, antimicrobial properties gained superior effect thanks to the uniform dispersion of carbon additives and fast electrical charge transfer [11]. Graphite additive is effective in conductivity of the polymer. Adding 0.5 % graphite to PVDF + 5 wt% Barium Titanate resulted in a 9.5 % increase in dielectric constant, a 50.4 % increase in capacitance, and a 8.58 % decrease in dielectric loss and a 4 % decrease in AC conductivity at the highest frequency of 2 MHz [12]. The presence of graphene-like fillers in a polymer matrix results in improvements in the physical, thermal and electrical conductivity of the polymer due to their structural properties. Carbon-based hybrid polymer composites have remarkable tensile strength, high Young's modulus and significant resistance to deformation due to the intrinsic strength, stiffness and strong interaction with other fillers-polymer matrix [13]. The young modulus and tensile strength of 2/24 wt% GNP/Carbon black added Ethylene–propylene–diene terpolymer rubber (EPDM) composite increased by approximately 195 % and 17 %, respectively [14]. In order to better utilize the large surface area and porous structure of expandable graphite, graphite foam was fixed to PVDF to obtain a composite. It provided high removal by adsorbing dye molecules with π-π interaction, hydrogen bonding and charge interaction between functional groups and dyes. EG doped PVDF effectively treat about 60 ml MB wastewater (10 ppm) per cubic centimeter with 200 L $m^{-2}h^{-1}$ flow velocity [15]. The acrylic resin polyethyleneglycol diacrylate supported graphite oxide and reduced graphite oxide were used for the removal of orange II and rhodemine B. While the GOx containing composite with showed good photocatalytic activity, dye removal decreased for rGO fixed polymer. Dye removal of rGO was due to adsorption, and since it did not show photocatalytic activity after fixing to the polymer, dye removal decreased [16].

While UV induced photocatalysis is highly effective compared to visible light and provides successful results in the degradation of microorganisms and pollution, it poses a threat to living tissues and rapid degradation of membrane materials. Owing to these drawbacks, photothermal effective particles have been developed as an alternative to UV induced filtration applications.

The photothermal (or plasmonic) effect occurs when electrons excited by visible or infrared light resonate and release heat energy. In addition, various reactions can be catalyzed in a similar way with photocatalysis. The photothermal mechanism could be initiated by interaction of the electron or the electron gaps formed with light exposure with the chemical in the environment. The most important component of the system are particles that can absorb near infrared rays (650–900 nm) with high efficiency and convert them into heat. Indocyanine green, some noble metals, carbon nanomaterial's, gold, silver, palladium, copper sulfide, some of the monolayer transition metals, dichalcogenides, graphene and its derivatives are examples of photothermal active particles [17–19]. The plasmonic effect of carbon nanotube and polypyrole coated melamine sponge (CNT)(m-CNT/PPy@MS) decreased the viscosity of the solution to be separated by increasing the temperature. Thus, the energy requirement for separation was reduced and the oil separation efficiency increased. With 1.0 kW/m^2 sunlight acting on the membrane, when the temperature increased to 118.6 °C, the separation time decreased by approximately 93 % compared to the normal membrane, while the adsorption increased 31 times [20]. Notably the Ce-MoO_3 catalyst degrades methylene blue 10 times more effectively than MoO_3 in the presence of visible light [21,22]. Au-Ag/WO_2.72/rGO nano photocatalyst was effective in the adsorption and photocatalytic degradation of dye impurities. The addition of Au and Ag plasmonic metals increased the photocatalytic efficiency of the composites at wavelengths of 420 nm and above [23]. The plasmonic effects of gold, graphene, carbon, lead, copper sulfate and some organic compounds have been used in the treatment of tumor cells. GO-PEG, Glucose-rGO, $ZnFe_2O_4$–rGO, PEG–GO/CuS, GO–$BaGdF_5$, rGO–Cu_2O were selectively distributed to cancer cells and heat release was achieved by interacting with NIR (808 nm) light. While the heat released inside the cell (50–60 °C) was effective in breaking down the protein structure of cancer cells, it did not cause any damage to other tissues and cells [19,24]. Gene therapy, hydrogen extraction from water, antimicrobial composites, and photothermal nanofluids are examples of other areas where plasmonic materials are used [25–27].

Plasmonic effective composites can be used in conventional filtration systems. Advantages such as flux control, degradation of impurities by creating electron holes, and increasing rejection efficiency with heat energy can be beneficial. Ag-TiO_2 binary metal composite prepared via an electrochemical method was effective in capturing electrons released from both Ag and TiO_2 and showed plasmonic activity. The chlorophenol degradation efficiency of sample containing 5 % Ag was recorded as 97 % [28]. Ag-TiO_2 was used to obtain hydrogen from water by photocatalytic effect, and 95 μmol H_2 yield was achieved with 79 nm sized TiO_2 particles at 457 nm irradiation.

One of the important parameters affecting the composite efficiency is particle size. Nanoscale small particles are frequently preferred due to their large surface area, quantum size and volume, as well as their biocompatibility, light absorption and antimicrobial properties [29]. AgNNp, which have good photocatalytic-photothermal properties, are produced using microorganisms, enzymes and plant extracts with green synthesis methods and offers eco-friendly, sustainable and low-cost alternatives. There are many physical and chemical methods applied for the synthesis of AgNNPs with many plants such as olive leave, cydonia oblonga seed, oak fruit hull (Jaft), aloe vera, green tea extracts. pH, temperature, settling time and extract content affect the activity of the particles in green synthesis methods [30]. Silver nanoparticles (SNPs) with an average size of 25 nm were prepared by quince petal aqueous extract and used as an antimicrobial agent for Erwinia amylovora bacteria [31]. Dyeing was done by absorbing aqueous extraction of quince leaves into wool fiber, then mordanted with $AgNO_3$ and $ZnCl_2$. Darker reddish-brown shades colored wool showing AgNNP formation showed the highest antimicrobial activity [32].

Graphite is the starting material of expanded graphene or graphene oxide, which belongs to the carbon family, and is frequently used in combination with metal oxides to obtain composites. There are few studies on the use of graphite as a composite additive with AgNP. In this study, AgNP prepared using quince seed extract according to the green synthesis method was combined with graphite and fixed to PVDF. Graphite-supported AgNP-PVDF (PAG) filtration membrane was prepared. While Ag is effective in absorbing infrared light, graphite ensures homogeneous dispersion of AgNP and an infrared sensitive functional composite membrane is obtained. The composites were characterized via XRD, FT-IR, SEM, PL analyses. The filtration performance of the obtained Ag-Gr-PVDF (PAG) composite membrane under specific infrared light (808 nm) was first tested in this study. Photothermal-plasmonic effective composite anchored PVDF membranes suitable for use in filtration under light-on and off conditions were prepared and applied as filtration material.

2. Materials and methods

2.1. Materials

The polymer matrix polyvinylidene fluoride PVDF (Solef 6010, MINGER) and solvent N, N-dimethylformamide, DMF (73.09 g/mol, 0.944 g/mL Sigma Aldrich) were used in analytical grade. Ethanol, (C_2H_5OH, pure, ≥95 %), sodium hydroxide (NaOH, ≥98 %), hydrochloric acid (HCl, ≥37 %) were obtained from Sigma Aldrich and used without any purification. For the synthesis of silver particles, $AgNO_3$ (169.87 g/mol, %99) was purchased from Sigma-Aldrich.

The reducing extract was obtained from quince (Cydonia Oblonga Miller) seed collected from the Osmaneli Town of Bilecik/Turkey in

October 2023. The samples were stored in polyethylene cups and kept at 4 °C in the laboratory. Before using, quince seeds were washed and wiped quickly to protect its extract. Double distilled water, methyl orange (MO, Orange III) and graphite (+100 mesh) were purchased from Sigma Aldrich and used without any purification. Bovine serum albumin, BSA (MW: 66,000 Da, ≥98 % purity, Sigma Aldrich) was used as model protein solution with boric acid, H_3BO_3 (MW: 61.83 g/mol, Sigma-Aldrich), phosphoric acid, H_3PO_4 (MW: 98 g/mol, Sigma-Aldrich) and acetic acid, CH_3COOH (MW: 60.05 g/mol, 99.7 %, Sigma-Aldrich) for pH adjustment.

2.2. Membrane preparation

Aqueous quince seed extract was obtained from whole seeds (10 g) using distilled water at 25 °C (water to seed mass ratio of 40:1). The mixture was stirred at 250 rpm for 3 h to scrape the extract. The mixture were then filtered with 80 mesh (200 μm) sieve to separate from seeds and insoluble residues. It was evaporated by low temperature (Heidolph 4000, 40 °C) until a concentration of approximately 90 % (v/v).

AgNPs particles were prepared by the precipitation method in casting solution. For this, the polymer solution was prepared by dissolving 1.6 g PVDF in 10 ml DMF solvent at 65 °C. A total of 0.16 g of ground silver salt was added to polymer solution. 5 ml quince extract was added drop vise and solution was mixed until color change was complete. After a dark brown color was obtained, the solution was homogenized by ultrasonic bath for 5 min. Then it was poured onto a 15x15 cm glass surface and sprouted out with a 300 μm applicator at 25 °C. After waiting for 10 s to stabilization glass was immersed in distilled water bath for phase separation. Excess silver ions were removed, the composites were washed and stored in water with 0.1 % hydrogen peroxide until analysis and filtration. Control samples were prepared by adding 0.16 g of graphite to the polymer solution of similar composition in the presence of silver + quince extract and without silver. Graphite powder was mixed for uniform distribution in the polymer solvent. The mixture was homogenized in an ultrasonic bath for 10 min. before being added to the casting solution. The preparation of silver particles was done as described above. The silver content of the composites was designed to be 10 % of the polymer mass. The amount of extract required to reduce the specified silver salt was determined by control experiments at different concentrations before adding it to the polymer solution. The obtained powder and particles formed inside polymer was called AgNP. The schematic representation of experimental steps of PVDF, Ag, graphite, Ag and graphite doped (P, PA, PG and PAG respectively) composites with filtration cell are shown in Fig. S1.

2.3. Characterization

The crystallinity of the structures was investigated in the range of 5-80° by XRD (Panalytical/Empyrean) analysis. The morphological structure of gold plated composites was imaged by SEM analysis at 10.00 kV (ZEISS/Supra 40 VP, Germany). The distribution of graphite-AgNP particles anchored on the PVDF was imaged with a Hitachi H 7650 transmission electron microscope (TEM) at 100 keV. Phc polymeric composite of 50 nm were placed on a copper grid using a microtome. Molecular interaction of polymer and additive was analyzed by FT-IR in the region between 4000 and 650 cm^{-1} with Perkin Elmer Frontier L128-0099 FT-IR ATR. The electron-hole pair recombination of composites was determined by photoluminescence spectrometer (Perkin Elmer FL6500, PV instruments) at the range of 355–900 nm wavelength. MO and BSA concentrations were determined by UV–visible spectrometer (PG instruments, T80) at 466 and 280 nm wavelength respectively. Surface hydrophilicity of samples was investigated by contact angle analyzer (KSV Attention, Finland) at room temperature.

The water uptake capacity (WU) were calculated to estimate water affinity of the samples. Membranes were weighted (W_w) after mopping with blotting paper. The samples were subsequently dried in a vacuum oven at 40 °C for three hours and it was weighted again (W_d). Water uptake capacities were calculated by Eq. (1).

$$WU(\%) = \frac{W_w - W_d}{W_w} \times 100 \tag{1}$$

The porosity percentages of membranes (PO%) was calculated by Eq. (2) to get knowledge about pores:

$$PO\,(\%) = \frac{W_w - W_d}{dA\delta} \times 100 \tag{2}$$

Where d is the density of distilled water ($kg.m^{-3}$) at 25 °C, A is membrane area (1.7×10^{-3} m^2) and δ is the thickness of wet membrane (m).

Pore radius was determined by Guerout-Elford-Ferry equation [20], Eq. (3).

$$r_m = \sqrt{\frac{(2,9 - 1,75\varepsilon)8\eta lQ}{\varepsilon.A.\Delta P}} \tag{3}$$

where r_m is average pore radius (nm), ε is porosity, η is viscosity of water (8.90×10^{-4} Pa.s) at room temperature, l represents membrane thickness (m) and Q is flow rate of water (m^3/s). A and ΔP mean effective area of membrane (m^2) and flux pressure (Pa) respectively. The thickness of the dried and wet membranes was tested by thickness measuring instrument (Hornbach, 0.25–0.01 mm range)

The pure water flux (PWF) performances of membranes were measured in an ultra-filtration cross flow membrane cell (designed for laboratory studies) with distilled water and calculated in $L.m^{-2}.h^{-1}.bar^{-1}$. Transmembrane pressures (TMP) of system were adjusted as 1.0, 1.5 and 2.0 bar after the membrane was for 8 h. The PWF was calculated by Eq. (4).

$$PWF = \frac{V}{At} \tag{4}$$

where V is amount of permeate (L), A is membrane area (1.7×10^{-3} m^2) and Δt is the filtration time (h). To better understand the compression behavior of the membrane under applied pressure compaction factor (CF) was calculated from the initial PWF/constant PWF value.

2.4. Rejection and antifouling experiments

The organic matter rejection performances of composite membranes (R%) were measured at ultra-filtration cross-flux membrane cell used for filtration experiments. A single lamp self-designed photo reactor with cooling equipment with an 8 W infrared lamp (2 × 2 cm, Philips, spectral range 808 nm) was used. A schematic representation of process is given in Fig. S1. MO used as a model pollutant for rejection experiments. For this purpose 50 mg/L MO solution was prepared by dissolving a certain amount of MO in distilled water. MO filtration was performed at a pH of approximately neutral (7.4). This pH value is the optimum value for MO removal and was determined by investigating the adsorption behavior of MO at different pH values in previous studies [33]. The BSA filtration performances of composites was also investigated with 0.5 g/L BSA into phosphate buffer solution (0.01 M, pH:7.4) as a pH stabilizer agent. Pure water, BSA or MO solution was pumped to membrane cell continuously by air pressure. A membrane with the effective filtration area of 1.7×10^{-3} m^2 was placed in the filtration cell. It was irradiated by one 8 W lamp at the distance of 5 cm. Initially the membrane was pre-pressed at 1.0 bar for 30/45 min. Pure water was used for stable permeation and the permeate was collected until compaction for 3 min. After the lamp was turned on, MO solution was provided into the membrane cell under infrared light at 0.5 bar for 90 min. The permeate was collected and MO concentration was determined by UV-spectrometer at 466 nm which was calculated by Eq. (5).

$$R(\%) = \left(1 - \frac{C_p}{C_f}\right) \times 100 \tag{5}$$

Where, C_p and C_f are the concentration of organic matter in permeate and feed solutions respectively. BSA rejection tests were conducted similarly to the MO experiments and, the concentration was analyzed via UV spectrometer at 280 nm.

2.5. Reusability studies

Three different fluxes were determined according to application order. PWF_1 means first water flux. After MO/BSA filtration, membranes were washed and immersed in distilled water for 5 min. Then PWF values of cleaned membranes were measured by pure water filtration again to calculate PWF_2. PWF_3 values of MO/BSA filtrated and light irradiated membranes were obtained by by pure water filtration. The flux recovery ratios of membranes (FRR) were calculated by Eq. (6).

$$\mathrm{FRR}(\%) = \left(\frac{\mathrm{PWF}_3}{\mathrm{PWF}_1}\right) \times 100 \tag{6}$$

Recycling performance of membranes was evaluated in 3-run filtration test. After washing and measuring the fouled flux, the membrane irradiated for 1 h to degrade the contaminants. The reversible, irreversible and total fouling rates were calculated by Eqs. (7)–(9) [34]

$$\mathrm{R_r}(\%) = \left(\frac{\mathrm{PWF}_3 - \mathrm{PWF}_2}{\mathrm{PWF}_1}\right) \times 100 \tag{7}$$

$$\mathrm{R_{ir}}(\%) = \left(1 - \frac{\mathrm{PWF}_3}{\mathrm{PWF}_1}\right) \times 100 \tag{8}$$

$$\mathrm{R_t}(\%) = \left(1 - \frac{\mathrm{PWF}_2}{\mathrm{PWF}_1}\right) \times 100 \tag{9}$$

The metal analysis in the $PWF_{1,\ 2,\ 3}$ effluents was conducted to determine leaching by analyzing the water using AAS (Perkin Elmer, PinAAcle 900 F).

3. Results and discussion

The XRD diffraction patterns of raw PVDF and composites are given in Fig. 1. The crystalline arrangement of PA and PG composites prepared with AgNP and graphite additives is significantly different from that of raw PVDF. The peak observed around $2\Theta = 20.3^\circ$ in all composites is due to the dominance of the beta phase of PVDF. The very low-intensity peaks indicate that the presence of alpha-phase PVDF in PA and PG largely disappeared in PAG. The beta phase peak of PAG also shifted to 21.1° [35,36]. It is understood from this that with additive anchoring to polymer, the crystal structure changes by partially compressing the gaps

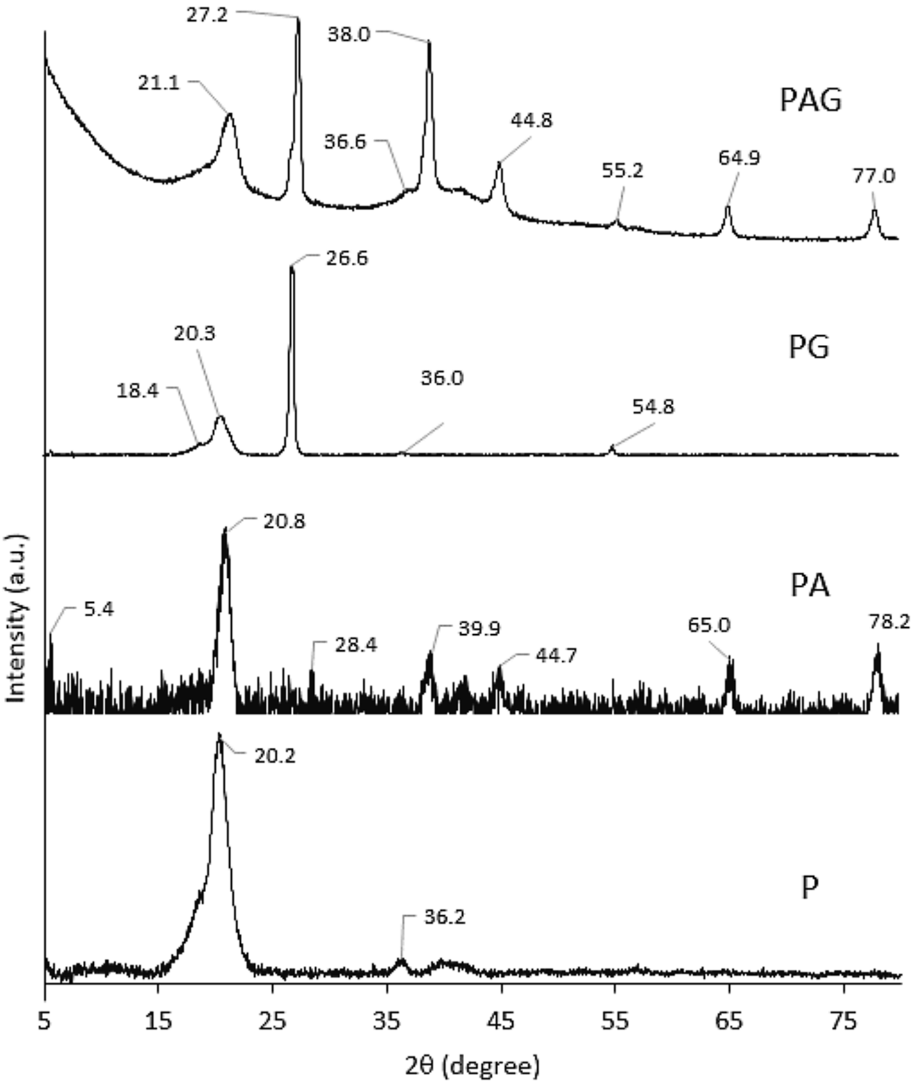

Fig. 1. XRD patterns of composites.

between the layers. The sharp peaks around 2Θ = 38, 44, 64 and 77° observed in the diffraction patterns of PA and PAG are the result of the presence of AgNP with compatibility of AgNP with polymer matrix [31,37,38]. The presence of graphite is evident from the sharp peak observed at 26.6° in PG and shifting to around 27.2° in PAG, which also indicates the narrowing of the interlayer distance. The presence of this sharp peak was interpreted as the interlayer distance being approximately 0.334 nm [39]. The peak observed around 54.8° in PG and PAG also indicates the presence of graphite, and its low intensity may be due to the homogeneous distribution of graphite. The changes in crystallinity recorded by presence of AgNP and graphite addition to the polymer indicate that the new composite has been successfully prepared.

Cross sectional and surface SEM images of composites are presented in the Fig. 2. The morphological structure of raw PVDF has been changed by AgNP, graphite and AgNP + graphite additives. Finger-like structures expanding from top to bottom were formed in all composites. However, changes have occurred in the formations of lengths and widths of these channels, which determine the membrane permeability and filtration performance. The additive type is the most important reason for these changes, and finger-like structures in PAs have extended downwards and exceeded half of the section compared to P. Additionally, the number of small channels on the upper surface of the PAs has increased. Unlike others, in PG composite, the formation of channels is minimal and, no small channels in the upper layer are formed. In this state, PG exhibited a more homogeneous distribution than raw PVDF. The interaction of PVDF and graphite effectively maintains the homogeneity of the structure during phase inversion The homogenizer effect of graphite was partially preserved in PAG and a uniform distribution and polymer network were achieved despite the presence of AgNP. This proves that the graphite additive is reasonable and should be applied to improve the AgNP light absorption effect. The favorable structure of the PAG composition is also evident from the surface images. The AgNP

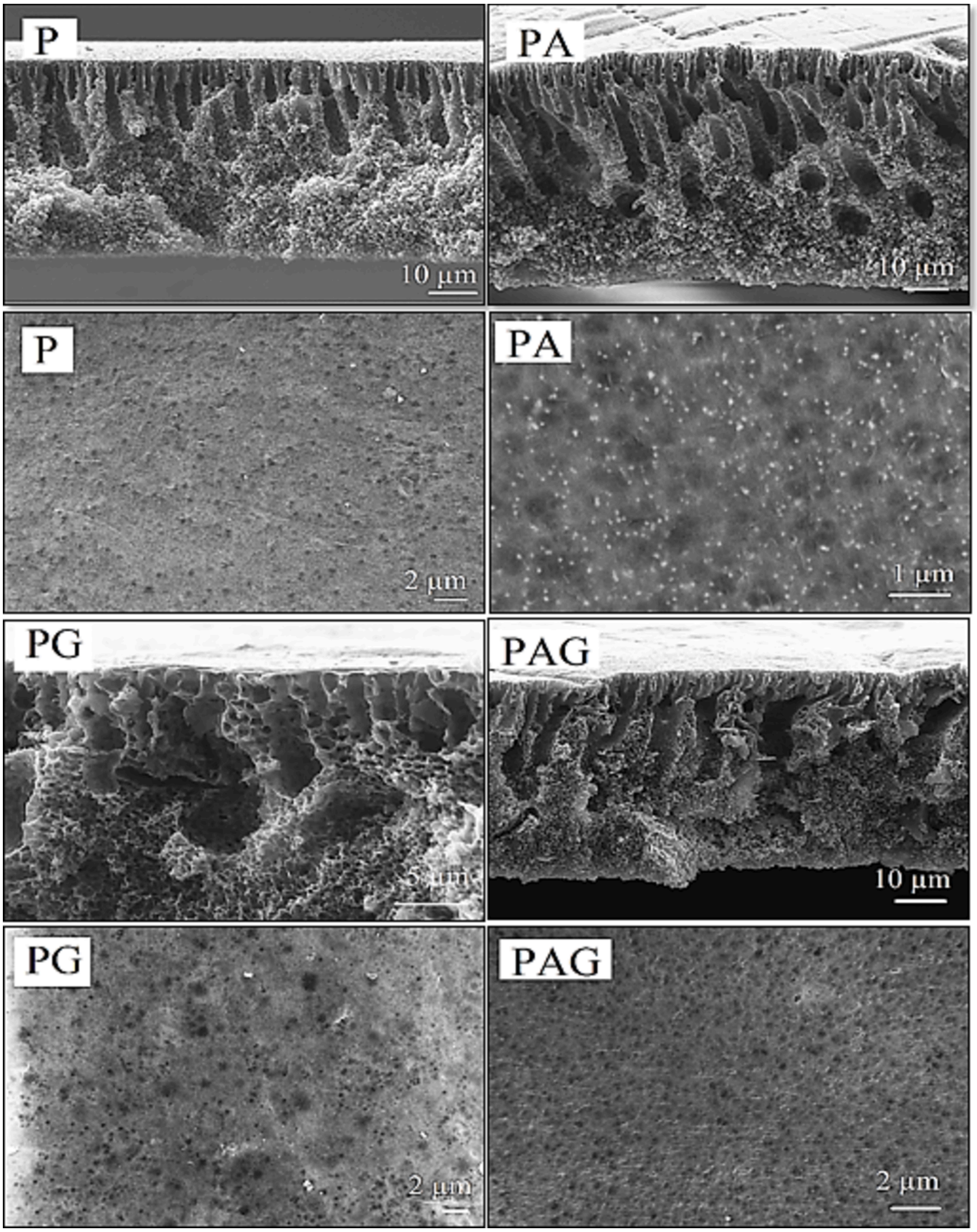

Fig. 2. Cross section and surface SEM images of composites.

particles observed on the PA surface were evenly distributed in the inner parts of the PAG. The PAG combination stands out as a structure in which light active particles are anchored to the polymer via the optimal route. In addition, the beginnings of finger-like channels observed at different sizes on the PG surface were more homogeneously distributed in the PAG. The elemental composition and EDX spectrum of the SEM image taken from the cross-sectional area of PAG are given in Fig. S2. The Ag content of 13.59 % is very close to the component ratio formed in the solution phase, indicating a suitable composition. A uniform distribution of AgNP can also be observed in the TEM images of hemispherical AgNP and PAG with dimensions of 35–45 nm Figs. S3 and S4. Temperature, settling time and acidity are the most important primary parameters that affect particle size and therefore particle activity.

Molecular interactions between PVDF and additives and structural changes were analyzed by FT-IR Fig. 3. Changes occurring in the range of 400–600 cm^{-1} in Ag-doped composites indicate Ag-O stretching vibrations. The vibrations of characteristic CH and CF_2 bond stretches of PVDF are represented by the 1400 and 879–1180 cm^{-1} bands, respectively. The distinct bands observed at 1070 and 838 cm^{-1} belong to the stretching of CF, CH bonds and remained unchanged in all the composites. The effect of AgNP addition on the crystal structure of the polymer can be understood from the decrease in the 765 cm^{-1} band intensity in PA and PAG, which indicates the alpha phase of polymer [40]. The alpha phase is preserved in the crystal structure of the polymer in the PG composite. In raw PVDF and other composites, the band corresponding to 1269 cm^{-1} shows that the beta phase is dominant [41]. The beta phase crystal arrangement of PVDF is a preferred form due to its superior physical and electrical conduction [42]. PAG composite has a combination of beneficial crystallinity, alpha and beta along with the homogeneous effect of graphite additive.

By analyzing the light emitted from excited electrons, the beam sensitivity of the composite was determined via the photoluminescence technique Fig. 4. PL density provides information about electron-hole pair recombination. A higher PL intensity indicates a longer gap between the two bands and therefore lower photocatalytic activity. The energy supplied to the absorber material causes the valence electrons to

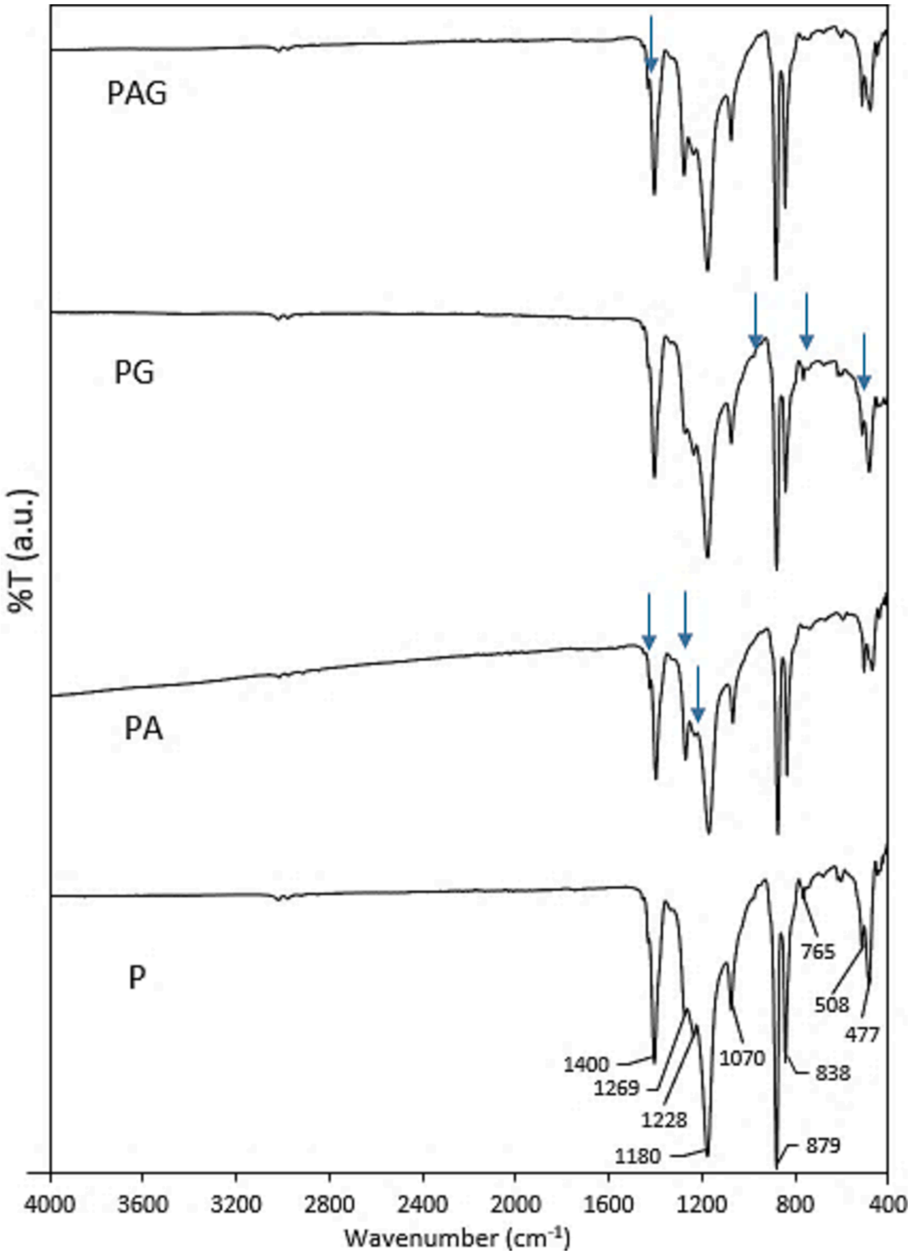

Fig. 3. FT-IR spectrums of composites.

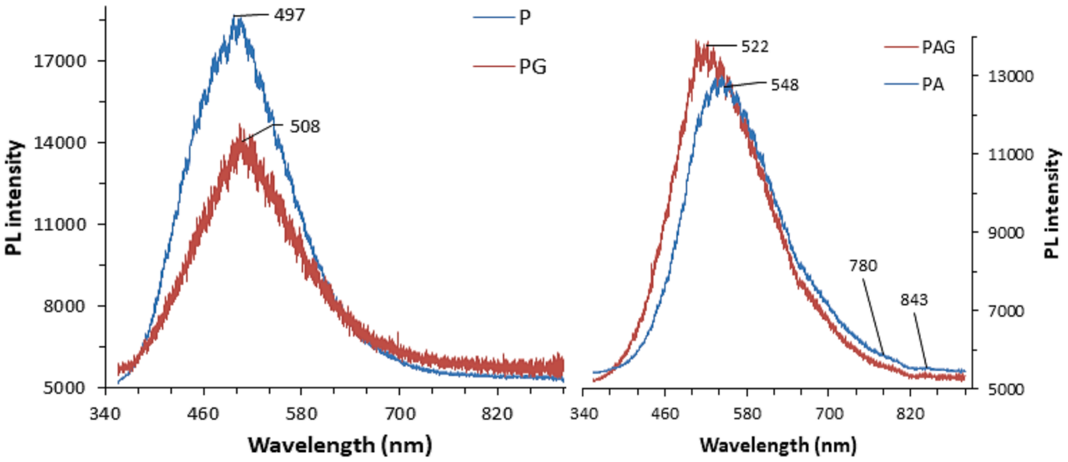

Fig. 4. Photoluminescence spectra of composites.

be excited and move to the conduction band. The place where the electron comes out is called defect sites, positively charged hole (h+). The number of excited electrons and holes increases in proportion to the energy applied to the semiconductor material. This recombination continues as long as energy is applied until all electrons are excited [34]. Compared with those of the PA and PAG composites, the intensities of the PL values measured for P and PG are quite high. This indicates that, the conduction bands become closer because of the AgNP in the structure of PA and PAG composites, and these are excited more easily in the presence of light. The intense and broad peaks observed in the 500–550 nm range are caused by reflected light and show the light-shielding effect of the polymer. PA prepared with AgNPs and PAG with AgNP and graphite additives showed absorbance at similar wavelengths in the visible and near infrared regions. Absorbance values were observed at 783 and 851 nm wavelengths in the PL spectrum of pure AgNP Fig. S5. By anchoring AgNP to the polymer, the absorbance properties of AgNP are successfully transferred to the polymer. The findings prove that the composites are sensitive in the presence of visible and near infrared light.

3.1. Physical properties of the membranes

The contact angle values, which are an indicator of hydrophilicity, are given in Table 1 along with pore radius, water uptake, and porosity percentage and compaction factor. The addition of AgNPs increased the hydrophobicity of the polymer. This occurred because AgNPs induced the formation of a smoother surface.. As the roughness decreased, the speed of water penetration from the surface into the pores also slowed down. That creates a higher water droplet on the membrane. The relationship between roughness and hydrophilicity was explained by examining AgNP-doped membranes of different sizes, and increasing the particle size to 33 nm effectively filled the voids on the surface and reduced roughness. The hydrophilicity of the smooth surface decreased as a result of larger and convenient area for water drop [43]. The smallest average pore radius was calculated as 41.5 nm with PA. The CA value decreased significantly in PG and PGA with the addition of graphite, and the membrane became more hydrophilic than that of PA.

Table 1
Physical performances of composites.

Sample	Contact Angle (°)	WU %	PO %	Pore Radius (nm)	Compaction Factor (CF)
P	74.1 ± 0.2	61	62	34	1.8
PA	82.3 ± 1.7	57	66.5	31.5	1.3
PG	72.5 ± 0.9	69	61	44	1.5
PAG	75.0 ± 0.1	63.5	65	37.2	1.4

Since the fluid character of graphite provides homogeneous distribution, larger pores are formed due to faster phase separation. This increased the rough structure and larger pore width of PG facilitating the entry of water droplets easily. In PAG, the opposing properties of AgNP (tend to smooth surface, high hydrophobic) and graphite additives against hydrophilicity are balanced by proceeding competitively. The WU% value of the PA decreased in proportion to its pore structure and hydrophilicity, which is highly compatible. While hydrophobicity was effective in reducing water uptake, this value was recorded as highest at 69 % for PG. At the same time, the most porous structure was obtained with PA according to PO% value of 66.5 %. These data that many small pores exist. Despite the widest pore radius of PG among all composites, its low porosity is reasonable. The WU and PO% values were 63.5 and 65 respectively in PAG, and the addition of graphite and AgNP resulted in the optimum combination. This shows that the pore size can be adjusted with graphite and an active metal-additive composite structure with the desired properties can be obtained. The compaction values and their durability were analyzed by dividing PWF_1 by PWF_2. Moreover, information was obtained about the space between the pores and the resistance of the membrane to filtration pressure. The highest CF value of the raw PVDF membrane indicates that the greatest compression occurs during filtration. This resulted from the large gaps in the structure of the membrane. Although the high flux value recorded in the first filtration is a positive feature, the pressure resistance of the membranes is necessary for both constant flux and filtration efficiency. It is understood from the CF value of PA that the voids in the structure are at the lowest level and compression as a result of filtration is minimal. It is understood that spherical AgNP particles disperse most tightly into the polymer during phase inversion, minimizing the formation of voids. Compared with those of P, the CF values of PG and PAG are more resistant to compression.. The large particles of the graphite additive were partially effective in the formation of large voids. However, this was tolerated by the presence of AgNP in PAG, and the formation of voids was balanced, and the CF value was obtained as 1.4. These values affect the separation efficiency of the membrane depending on the solution type. More hydrophobic structures with relatively small pores are favorable for the separation of organic substances from the aqueous environment. In addition, hydrophilicity becomes important in catalytic processes where water-soluble structures are required for easy transportation of substrate to active sites [44,45].

3.2. Flux, rejection and antifouling performances of composites

The pure water flux performance of the membranes was tested at three different pressure Fig. 5. There was a linear increase in the fluxes of all the membranes with increasing pressure from 1 to 1.5 bar. At all

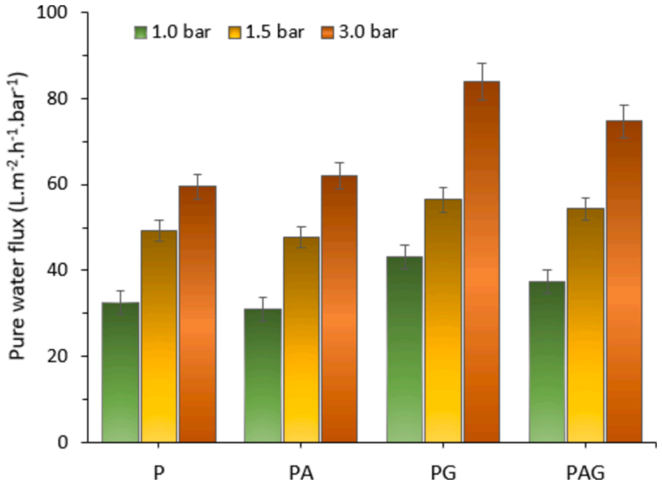

Fig. 5. Pure water flux performances of composites at different pressures. Test conditions: membrane area = 1.7×10^{-3} m^2, filtration time = 0.5–1 h.

pressure values, the highest water flux of 84 $L.m^{-2}.h^{-1}.bar^{-1}$ was obtained with PG at 3 bar. This result is well compatible with the physical properties of the membrane. As a result of the increasing pressure, the first blockage occurred at P. PA and PAG showed an average change in pressure changes, exhibiting a flux of 62 and 74.7 $L.m^{-2}.h^{-1}$.bar at a pressure value of 3 bar. The flux of PAG is within the range of P and the flux of composites indicates that the composite composition and structure are well ordered. Compared to raw PVDF (59.5 $L.m^{-2}.h^{-1}.bar^{-1}$at 3 bar), it is understood that the fluxes of AgNP and graphite incorporated membranes increased, while AgNP alone exhibits lower flux (47.8 at 1.5 bar). This is probably the result of the hydrophobic character of AgNP compared with others resulting from its smooth structure [46]. The decrease in flux with increasing pressure indicates that the voids in the structure collapse and compress. However, it is understood from the flux values that there is no sudden compression in PG and PA. Particulate additives prevented this collapse by increasing the resistance of the polymer's filtration channels (1) and creating smaller pores (2). While graphite additive induced the formation of large pores, AgNP was effective in the formation of smaller pores. The combination of two additives in the same composite ensures in equal distribution of these properties, and the average flux value is obtained with the PAG membrane. The distribution of finger-like transfer channels triggered by AgNP was homogeneous distribution with graphite, thus providing optimal pure water flux. The high porosity value tolerated the restriction caused by the compression of additive.

In Fig. 6b and c normalized values of 10 and 50 mg/L MO solution filtration of different membranes are given (PWF_1/PWF_0) with the normalized values of three different runs. Compared with P and PG, PA and PAG membranes were beneficial during the 120 min removal period, especially at low MO concentration. The increase in PG performance was due to the improved hydrophilicity and homogeneous distribution with the favorable additive ratio and therefore the increased filtration ability. AgNPs effectively oxidize of organic molecules in the presence of infrared light. This effect is due to the light absorption of particles and the effective transfer of light-excited charges. Therefore, PA and PAG presented a higher and more stable fluxes than the others in the presence of 10 mg/L MO. The increasing amount of organic matter caused a decline and instability in the flux performance of all membranes.

3-run recycling filtration with normalized flux values of the membranes is presented in Fig. 6a. In each run, direct MO filtration, filtration after rinsing and filtration at light irradiation were carried out. After 3 runs, the normalized flux values of the PA, PG and PAG membranes became more stable than those of P. The increasing flux value after each washing indicated that the organic contaminants accumulated on the surface are weakly attached to the surface. Flux values increased further with infrared light in PA and PAG. These findings indicate that light exposure provides self-cleaning properties in AgNP-doped membranes. The small increases observed in the normalized flux value of P at different steps are due to the cleaning effect by the applied steps. However, the combination of AgNP and graphite showed a more stable performance for recycling compared with performance of P. These results indicate that AgNPs effectively catalyze organic impurities. Unlike the addition of other photocatalyst, the addition of AgNP to polymer resulted in increased filtration efficiency owing to the surface plasma effect and the light sensitivity of the composite membrane.

The surface temperatures of the composites as a result of infrared light exposure for 10 min were recorded in dry and aqueous environments with infrared temperature (Medisana, precision: ±0.1 °C) for 10 min. Fig. S6. While the surface temperature of PAG composite increased from 26.5 °C to 36.5 °C, the temperature of PA changed to 30.9 °C only. A small changes was observed on the surface temperature of PG and P due to the heat of the light source. The temperature increase recorded on the PA and PAG surface as a result of 10 min of light exposure was due to the light sensitivity of the composites [47]. Composites that respond faster to light exposure and provide more photothermal conversion can be developed with improvements in parameters such as beam power, additive amount, and pore structure. The importance of this study is the successful preparation of infrared light responsive composites.

The possible mechanism of MO removal occurring on the composite surface with the synergistic effect of Ag graphite additives proceeded through the photocatalytic-photothermal mechanism. The electrons (e−) leaving the solid as a result of the light radiation exposure of the AgNP-graphite combination and the holes (h+) created by these electrons interact with the molecules in the environment. In addition to the e−/h+ electron-hole pair, the radicals formed by the oxidizing molecules such as oxide, hydroxide or peroxide as a result of the electron-hole pair interaction decompose organic pollution. Radical formation can proceed via many different initiators such as light, chemical or active metals. The reaction of the Fenton process initiated by light and proceeding via iron derivatives is an example of this. The radicals formed as a result of the interaction of Fe^{2+} ion/peroxide and oxygen molecule/e− in the PFb composite structure have shown effectiveness in organic removal [48,49]. The photocatalytic degradation mechanism of MO carried out by PA, PG and PAG composites is given in Fig. S1.

While AgNPs are effective in organic decomposition, graphite is active in the formation of homogeneous structure and increasing the efficiency of light absorption. In particular, keeping the thermal energy in the structure and ensuring its equal distribution with graphite made it easier for the substrate to reach the pores. An effect similar to thermal energy accelerating the flux by reducing viscosity in oil/water filtration was encountered here in the form of rapid advancement of MO [20]. Moreover, the induced electron transfer also accelerated with elevated temperature. Thus, the penetration of possible oxy and hydroxy radicals increased with the degradation of MO, a source of organic pollution. The photothermal effect can be understood from the resistance of PA and PAG membranes to fouling, which is one of the biggest problems in filtration membranes In addition, TOC analysis was performed to determine whether organic matter removal was based solely on filtration. For this purpose, the TOC values of the filtration solution and the initial concentration of 10 mg/L MO were compared. Table 2 shows that some of the filtration eluent was catalyzed and broken down. In a continuous flow system, these values are quite valuable compared to traditional filtration efficiency. While some of the MO is separated by adhering to the structure as a result of filtration-adsorption, some of it may be broken down into acetate, water and carbon dioxide. While almost no degradation was recorded with P, PA and PAG membranes exhibit a catalytic effect in the presence of light. Efficiency can be further increased with parameters such as additive amount, light intensity and different oxidizing agents (such as H_2O_2). Light induced structures are superior to traditional filtration methods based on

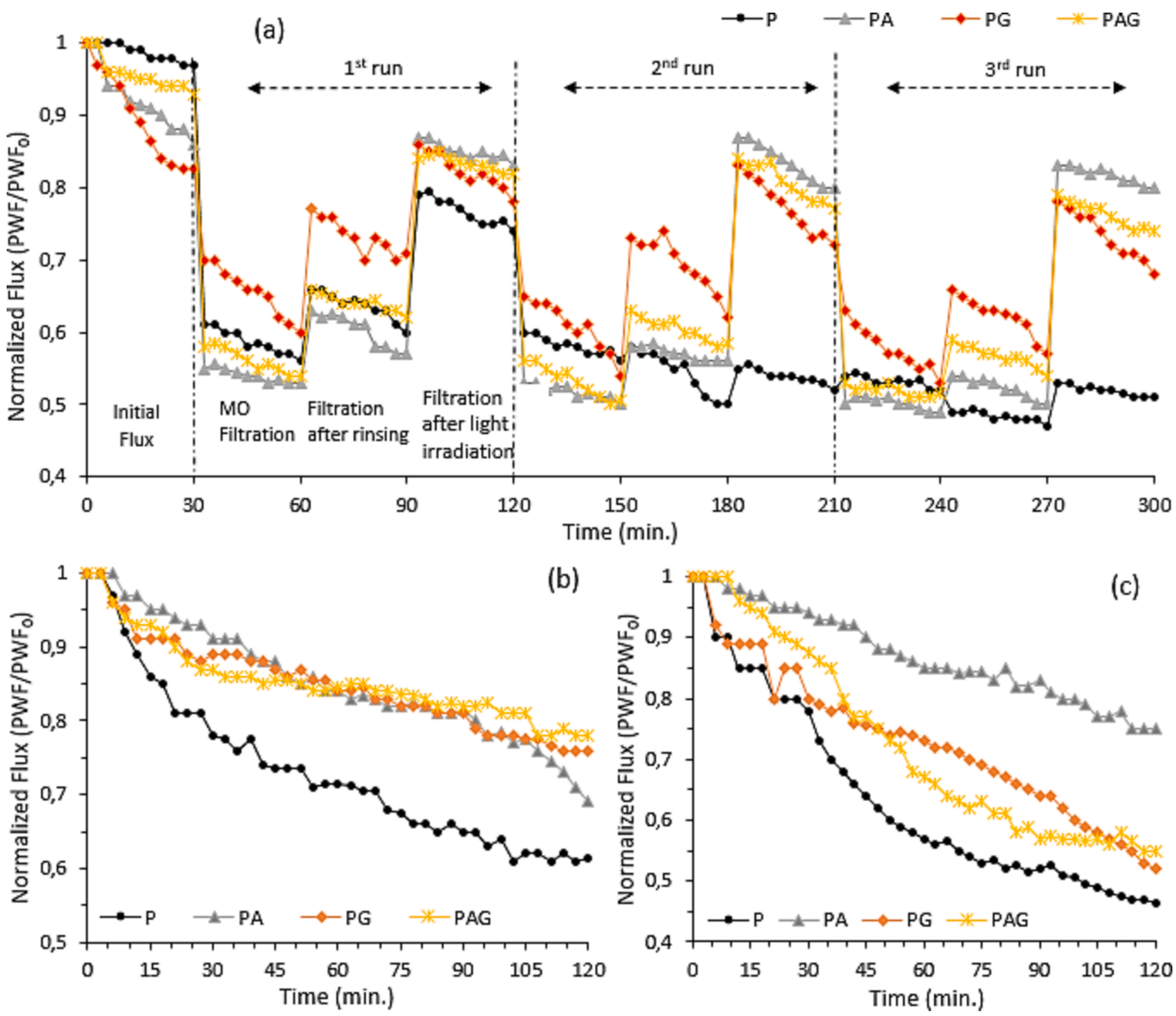

Fig. 6. Normalized flux values of time-dependent MO rejection on composite membranes during 3-run recycling, MO filtration, 5 min. water rinsing and light irradiation for 1 h. (a), normalized flux values of composites for 10 mg/L (b) and 50 mg/L (c) MO concentrations on under light irradiation. Test conditions: membrane area = 1.7×10^{-3} m^2, pressure = 0.5 bar, one 8 W Xe lamp (λ = 808 nm).

Table 2
Mineralization % and decolorization% of MO on light sensitive composite membranes.

Sample	Decolorization (%)	Mineralization (%)
P	5.8	0.7
PA	11.3	3.5
PG	9.7	1.7
PAG	13.5	3.8

adsorption.

The reversible, irreversible and total fouling performances of the membranes were calculated along with the FRR values Fig. 7. The FRR values of composite membranes are more stable and higher than those of P. For example, the FRR of PA was obtained as 86 % in the 1st run, and only a 4 % decrease was observed in the 3rd run. However, the FRR of P sharply decreased from 77.8 % to 52.5 %. These data provide information about total fouling, which is an indicator of the reusability efficiency of the membrane. After the 3rd run, the reversible fouling of P decreased unlike that of the composites, and the total fouling increased noticeably. Although the irreversible fouling values of PAG are unstable, the total fouling decreased and it was recorded as 22.4 %. These results indicate the self-cleaning ability of the AgNP additive composites is effective. The results supporting the anti-fouling performance can be seen from the rejection data during the 3-run Fig. 7. The rejection performance of composite were found to be higher than performance of P. This reveals that AgNP and graphite incorporation improved the structural properties with light-sensitive effect of AgNP. The decrease in the rejection efficiency of PG can be attributed to its wide gap permeable structure and lack of light sensitivity.

In terms of the irreversible and reversible values, filtration under light exposure is much more effective than the water washing process. All the membranes maintained their physical durability during the recycling period but exhibited different efficiencies. In addition, fouling, one of the biggest problems in filtration applications, is inevitably infested. While the type of additive significantly affects all properties of the membrane, the amount of additive should be investigated separately for each composite. The rejection performance of membranes changed

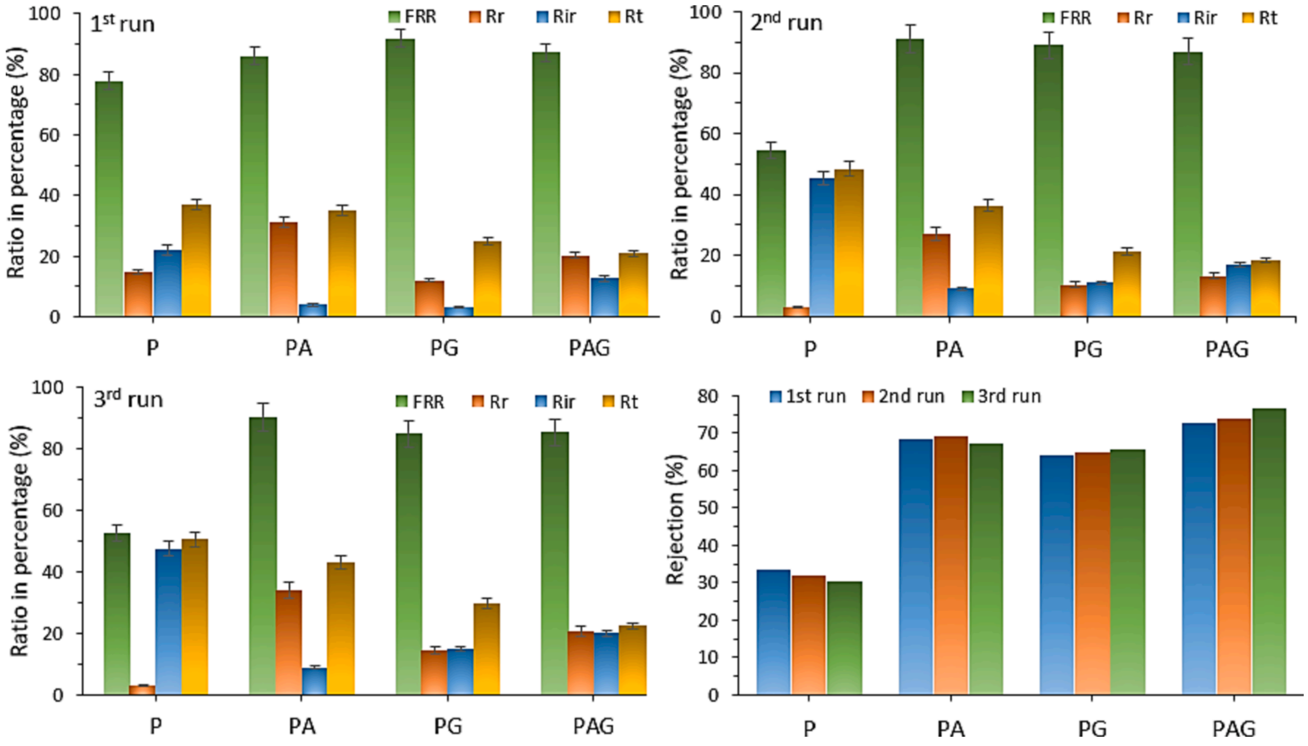

Fig. 7. Flux recovery ratio (FRR), reversible (Rr), irreversible (Rir) and total fouling ratios of composites for 3-run recycling with MO rejection efficiencies. Test conditions: membrane area = 1.7×10^{-3} m^2, compression pressure: 1 bar, 1000 mL 10 mg/L MO solution, pressure = 0.5 bar, one 8 W Xe lamp (λ = 808 nm).

with direct light exposure. Photocatalytic effect have a significant importance on improving membrane properties compared to the effect of just the additive type and amount. As a result of the metal analysis performed with calibration solutions in the range of 1×10^{-3}-1×10^{-5} mol/L in the filtration waters, no metal ions were detected.

To elucidate the mechanism of methyl orange removal, the change in the composite surface was analyzed by FT-IR at the molecular level Fig. S7. Clearly different from the IR spectra of PVDF and composites, the 1700–1800 cm^{-1} bands indicate the carbonyl groups of bonded MO derivatives. This is a proof that substrate adsorption is inevitably effective in filtration. Light-induced electrons, oxidation agents and holes interact with molecules adsorbed on the surface and remove pollution. Thermal energy generated by the light effect has the potential to prevent organic destruction and fouling by accelerating the substrate's transformation to active areas. As a result of light exposure and MO adsorption, crystallinity of the polymeric structure is predominantly amorphous. This shows the deterioration of the structure with the release of energy and chemicals as a result of continued use.

The prepared composite membranes have potential as filtration materials with and without light. Additives added to the polymer provided improvement in pore size, pore distribution and physical properties as well as light sensitivity. The flow behavior of the membranes was investigated by different molecules in different sizes. Therefore, the filtration capabilities of the membranes were tested in the presence of BSA. The experiment conditions were set as in MO rejection. From the normalized flux graphic, flux decreased sharply. There is more accumulation as a result of BSA filtration than of MO rejection Fig. 8. The large molecular structure of BSA accumulates in pores and accelerates clogging. Rapid blockage occurred after the first BSA filtration, especially in PA, which consists of many small molecules. The blockage in P and PG is partially less than the othersbecause these two membrane structures are more permeable and have a larger cross-sectional area

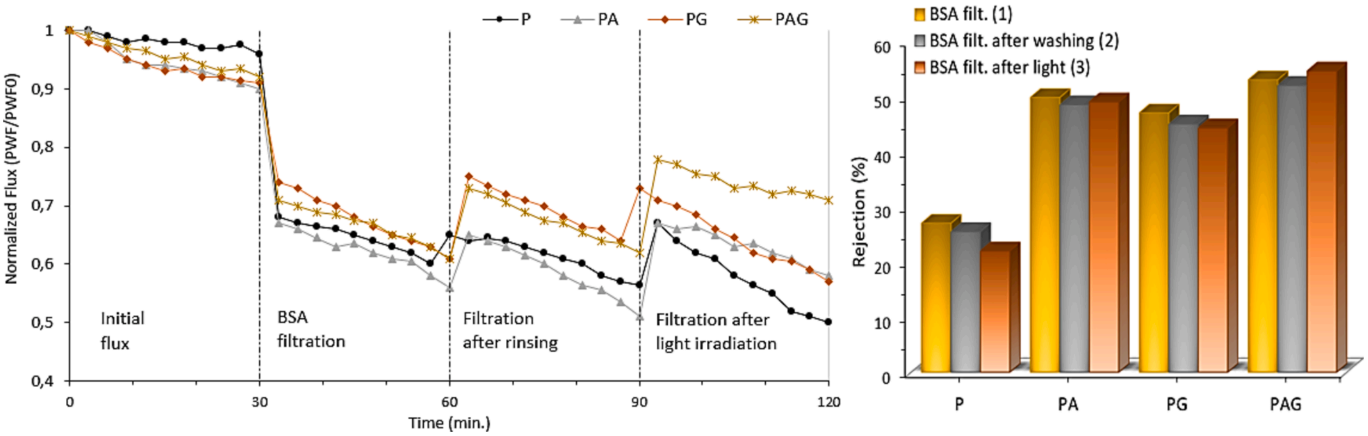

Fig. 8. Normalized flux values of time-dependent BSA rejection on composite membranes, BSA filtration, 5 min. water rinsing and light irradiation for 1 h. with BSA rejection%. Test conditions: membrane area = 1.7×10^{-3} m^2, 1000 mL 10 mg/L BSA solution, pressure = 0.5 bar, one 8 W Xe lamp (λ = 808 nm).

than the other structures. Fluxes after pure water washing are informative about the adhesion of impurities to the surface.

The adhesion of BSA molecules on the surface of PG and PAG is weaker than the others and therefore these molecules are easily removed from the surface by washing. Although the smooth surface provided by AgNP largely prevented the adhesion of BSA molecules to the surface, the blockage of PA resulted from organic impurities settling in small pores that could not be removed by washing. The flux performances of composite membranes even those not activated with light is considerable for use in traditional filtration processes. The change in the flux of composites as a result of light exposure is decisive for the importance of light responsive mechanism. In particular, as a result of light activation of PA and PAG membranes, their flux increased significantly compared to the others and reached the water washing values of PA and PAG. While a partial increase was recorded in PG, the blockage in P becomes deeper. Light activation increased the flux rate of the composite membranes which contains infrared responsive particles.

To understand the effect of the improvement in flux rate on BSA rejection performance, the BSA concentration in the permeated solution was analyzed. The BSA rejection rate of composite membranes was recorded to be greater than 50 % that was approximately 2 times higher than rejection% of P. Consistent with the flux values, BSA rejection% increased for light responded PA and PAG, while they decreased in the others. The stability of the rejection% rate is valuable for filtration efficiency, and the composites maintained this efficiency in terms of BSA rejection with light exposure. FT-IR analysis of BSA filtrated PAG was performed to elucidate the interaction between organic matter and the polymer surface Fig. S8. The band observed around 1656 cm^{-1} and recorded differently from the raw FT-IR spectrum of PAG (Fig. 3) corresponds to carbonyl stretching vibration [50]. BSA and other organic impurities form an adhered cake layer on the membrane surface, blocking the pores and causing a decrease in both flux and separation performance and membrane wear. The FT-IR band indicating the presence of BSA proves that it is inevitably adsorbed on the membrane surface. The pollution that accumulated on the surface to be degraded by photon activation induced by light activation. AgNPs were effective in the formation of light sensitivity, roughness and small pores, and graphite was effective in activating this sensitivity as well as in homogeneous pore distribution. Thus, on the composites, both the adhesion of organic molecules to the surface and the destruction of adsorbed molecules were slower than those on raw PVDF.

4. Conclusion

Infrared responsive AgNP doped composite membranes were prepared by solution precipitation and phase inversion methods. AgNPs were precipitated via the in-situ green synthesis method using quince seed extract in polymer solution. This method provided uniformly dispersed AgNPs preparation. In this study where photothermal applications were adapted to filtration, better antifouling and rejection were obtained with PA and PAG membranes under infrared light for MO and BSA rejection. The surface bond of the pollutant adsorbed on the surface were weakened and destroyed by photo-induced plasma effect. Thus, the formation of the cake layer causing blockage on the surface was reduced. The rejection-antifouling performance obtained at low light intensity can be improved by increasing the amount of solid fixed to the polymer and increasing the energy. In addition, the PL spectrum revealed that AgNP doped composites are suitable for activation at different light wavelengths. While the prepared composite membranes exhibit better filtration performance than raw PVDF even in the absence of light. Increasing the additive amount and light intensity can provide better antifouling and filtration performance. This study includes theoretical findings for the design of sustainable antifouling membranes operating with light activation.

Ethical Approval

Not applicable.

Authors' contributions

The authors declare that they have no conflicts of interest. All authors contributed to the study conception and design. Material preparation, data collection and analysis, the first draft of the manuscript was written by Huseyin Gumus and commented on previous versions of the manuscript.

Availability of data and materials

X-ray diffraction datasets were given as raw and interpreted in this study. XRD, FT-IR and PL graphs were created directly using raw analysis data [51].

CRediT authorship contribution statement

Huseyin Gumus: Writing – review & editing, Writing – original draft, Supervision, Funding acquisition, Data curation, Conceptualization.

Funding

This work was financially supported by TUBİTAK (Scientific and Technological Research Council of Turkey) with grant number 222Z333.

Declaration of competing interest

The authors declare the following financial interests/personal relationships which may be considered as potential competing interests: Huseyin Gumus reports financial support was provided by Scientific and Technological Research Council of Turkey (TUBİTAK) with 222Z333 grant number. If there are other authors, they declare that they have no known competing financial interests or personal relationships that could have appeared to influence the work reported in this paper.

Appendix A. Supplementary data

Supplementary data to this article can be found online at https://doi.org/10.1016/j.jphotochem.2024.116160.

Data availability

Data will be made available on request.

References

[1] R. Rath, P. Kumar, L. Unnikrishnan, S. Mohanty, S.K. Nayak, Functionalized poly (vinylidene fluoride) for selective proton-conducting membranes, Mater. Chem. Phys. 260 (2021) 124148, https://doi.org/10.1016/j.matchemphys.2020.124148.

[2] N. Pezeshk, R.M. Narbaitz, More fouling resistant modified PVDF ultrafiltration membranes for water treatment, Desalination 287 (2012) 247–254, https://doi.org/10.1016/j.desal.2011.11.048.

[3] J. Mansouri, S. Harrisson, V. Chen, Strategies for controlling biofouling in membrane filtration systems: challenges and opportunities, J. Mater. Chem. 20 (22) (2010) 4567–4586, https://doi.org/10.1039/B926440J.

[4] L. Liu, L. Huang, M. Shi, W. Li, W. Xing, Amphiphilic PVDF-g-PDMAPMA ultrafiltration membrane with enhanced hydrophilicity and antifouling properties, J. Appl. Polym. Sci. 136 (42) (2019) 48049, https://doi.org/10.1002/app.48049.

[5] F. Edwie, M.M. Teoh, T.-S. Chung, Effects of additives on dual-layer hydrophobic–hydrophilic PVDF hollow fiber membranes for membrane distillation and continuous performance, Chem. Eng. Sci. 68 (1) (2012) 567–578, https://doi.org/10.1016/j.ces.2011.10.024.

[6] P.S. Goh, A.F. Ismail, B.C. Ng, Carbon nanotubes for desalination: Performance evaluation and current hurdles, Desalination 308 (2013) 2–14, https://doi.org/10.1016/j.desal.2012.07.040.

[7] Z.-K. Li, W.-Z. Lang, W. Miao, X. Yan, Y.-J. Guo, Preparation and properties of PVDF/SiO2@GO nanohybrid membranes *via* thermally induced phase separation

method, J. Membr. Sci. 511 (2016) 151–161, https://doi.org/10.1016/j.memsci.2016.03.048.

[8] I.J. Ani, U.G. Akpan, M.A. Olutoye, B.H. Hameed, Photocatalytic degradation of pollutants in petroleum refinery wastewater by TiO2- and ZnO-based photocatalysts: Recent development, J. Clean. Prod. 205 (2018) 930–954, https://doi.org/10.1016/j.jclepro.2018.08.189.

[9] J. Wang, et al., Earth-abundant transition-metal-based bifunctional catalysts for overall electrochemical water splitting: A review, J. Alloy. Compd. 819 (2020) 153346, https://doi.org/10.1016/j.jallcom.2019.153346.

[10] C.L. Muhich, J.Y.I. Westcott, T. Fuerst, A.W. Weimer, C.B. Musgrave, Increasing the Photocatalytic Activity of Anatase TiO2 through B, C, and N Doping, J. Phys. Chem. C 118 (47) (2014) 27415–27427, https://doi.org/10.1021/jp508882m.

[11] A. Abdel-Karim, et al., High flux and fouling resistant flat sheet polyethersulfone membranes incorporated with graphene oxide for ultrafiltration applications, Chem. Eng. J. 334 (2018) 789–799, https://doi.org/10.1016/j.cej.2017.10.069.

[12] S. Ali, H. Ali, M. Afaq, K. Mehmood, M. Uzair, W. Ahmad, Influence of barium titanate and graphite on electrical attributes of Polyvinylidene fluoride matrix composites, Mater. Sci. Semicond. Process. 181 (2024) 108606, https://doi.org/10.1016/j.mssp.2024.108606.

[13] W. Li, X. Li, Y. Li, Microstructure and properties of carbon fiber-H62 brass matrix composites prepared by friction stir processing, J. King Saud Univ. - Sci. 35 (5) (2023) 102652, https://doi.org/10.1016/j.jksus.2023.102652.

[14] L. Valentini, et al., Synergistic effect of graphene nanoplatelets and carbon black in multifunctional EPDM nanocomposites, Compos. Sci. Technol. 128 (2016) 123–130, https://doi.org/10.1016/j.compscitech.2016.03.024.

[15] H.-M. Song, L.-J. Zhu, M.-X. Shi, A.-Y. Li, Y.-Y. Sun, Functionalized expanded graphite foam supported by PVDF skeleton for cationic dyes selectively separating and purifying, Colloids Surf. Physicochem. Eng. Asp. 703 (2024) 135368, https://doi.org/10.1016/j.colsurfa.2024.135368.

[16] P. Avetta, M. Sangermano, M. Lopez-Manchado, P. Calza, Use of graphite oxide and/or thermally reduced graphite oxide for the removal of dyes from water, J. Photochem. Photobiol. Chem. 312 (2015) 88–95, https://doi.org/10.1016/j.jphotochem.2015.07.015.

[17] Z. Bao, X. Liu, Y. Liu, H. Liu, K. Zhao, Near-infrared light-responsive inorganic nanomaterials for photothermal therapy, Asian J. Pharm. Sci. 11 (3) (2016) 349–364, https://doi.org/10.1016/j.ajps.2015.11.123.

[18] A.S.C. Gonçalves, C.F. Rodrigues, A.F. Moreira, I.J. Correia, Strategies to improve the photothermal capacity of gold-based nanomedicines, Acta Biomater. 116 (2020) 105–137, https://doi.org/10.1016/j.actbio.2020.09.008.

[19] K. Li, M. Lu, X. Xia, Y. Huang, Recent advances in photothermal and RNA interfering synergistic therapy, Chin. Chem. Lett. 32 (3) (2021) 1010–1016, https://doi.org/10.1016/j.cclet.2020.09.010.

[20] X. Wu, et al., Photothermal and Joule heating-assisted thermal management sponge for efficient cleanup of highly viscous crude oil, J. Hazard. Mater. 403 (2021) 124090, https://doi.org/10.1016/j.jhazmat.2020.124090.

[21] M. Kang, Y. Kim, Photothermal reduction of 4-nitrophenol using rod-shaped core–shell structured catalysts, J. Ind. Eng. Chem. 86 (2020) 61–72, https://doi.org/10.1016/j.jiec.2020.01.028.

[22] Z. Liu, Y. Jin, F. Teng, X. Hua, M. Chen, An efficient Ce-doped MoO3 catalyst and its photo-thermal catalytic synergetic degradation performance for dye pollutant, Catal. Commun. 66 (2015) 42–45, https://doi.org/10.1016/j.catcom.2015.03.017.

[23] B. Li, X. Shao, T. Liu, L. Shao, B. Zhang, Construction of metal/WO2.72/rGO ternary nanocomposites with optimized adsorption, photocatalytic and photoelectrochemical properties, Appl. Catal. B Environ. 198 (2016) 325–333, https://doi.org/10.1016/j.apcatb.2016.06.001.

[24] Y.-W. Chen, Y.-L. Su, S.-H. Hu, S.-Y. Chen, Functionalized graphene nanocomposites for enhancing photothermal therapy in tumor treatment, Adv. Drug Deliv. Rev. 105 (2016) 190–204, https://doi.org/10.1016/j.addr.2016.05.022.

[25] H. Jin, G. Lin, L. Bai, A. Zeiny, D. Wen, Steam generation in a nanoparticle-based solar receiver, Nano Energy 28 (2016) 397–406, https://doi.org/10.1016/j.nanoen.2016.08.011.

[26] H.E. ElZorkany, T. Youssef, M.B. Mohamed, R.M. Amin, Photothermal versus photodynamic treatment for the inactivation of the bacteria *Escherichia coli* and *Bacillus cereus*: an *in vitro* study, Photodiagn. Photodyn. Ther. 27 (2019) 317–326, https://doi.org/10.1016/j.pdpdt.2019.06.020.

[27] Y. Zhou, et al., Controlled heterogeneous water distribution and evaporation towards enhanced photothermal water-electricity-hydrogen production, Nano Energy 77 (2020) 105102, https://doi.org/10.1016/j.nanoen.2020.105102.

[28] N.F. Jaafar, A.A. Jalil, S. Triwahyono, Visible-light photoactivity of plasmonic silver supported on mesoporous TiO2 nanoparticles (Ag-MTN) for enhanced degradation of 2-chlorophenol: Limitation of Ag-Ti interaction, Appl. Surf. Sci. 392 (2017) 1068–1077, https://doi.org/10.1016/j.apsusc.2016.09.112.

[29] A.W. Alshameri, M. Owais, Antibacterial and cytotoxic potency of the plant-mediated synthesis of metallic nanoparticles Ag NPs and ZnO NPs: A review, OpenNano 8 (2022) 100077, https://doi.org/10.1016/j.onano.2022.100077.

[30] M.R. Khan, M.A. Urmi, C. Kamaraj, G. Malafaia, C. Ragavendran, M.M. Rahman, Green synthesis of silver nanoparticles with its bioactivity, toxicity and environmental applications: A comprehensive literature review, Environ. Nanotechnol. Monit. Manag. 20 (2023) 100872, https://doi.org/10.1016/j.enmm.2023.100872.

[31] S. Tarighi, M. Soltani Nejad, Ecofriendly fabrication of silver nanoparticles using quince petal extract and its antibacterial properties against fire blight disease, *J. Nat. Pestic. Res.*, 4 (2023) 100026, 10.1016/j.napere.2023.100026.

[32] A. Cerempei, E.I. Mureşan, N. Cimpoeşu, C. Carp-Cărare, C. Rimbu, Dyeing and antibacterial properties of aqueous extracts from quince (*Cydonia oblonga*) leaves, Ind. Crop. Prod. 94 (2016) 216–225, https://doi.org/10.1016/j.indcrop.2016.08.018.

[33] H. Gümüş, B. Büyükkıdan, Pollution removal performance of chemically functionalized textile waste biochar anchored poly(vinylidene fluoride) adsorbent, *J. Turk. Chem. Soc. Sect. Chem.*, 9(3) (2022) 3, 10.18596/jotcsa.1026303.

[34] Z. Chen, et al., Photocatalytic antifouling properties of novel PVDF membranes improved by incorporation of SnO2-GO nanocomposite for water treatment, Sep. Purif. Technol. 259 (2021) 118184, https://doi.org/10.1016/j.seppur.2020.118184.

[35] H. Gumus, Performance investigation of Fe3O4 blended poly (vinylidene fluoride) membrane on filtration and benzyl alcohol oxidation: Evaluation of sufficiency for catalytic reactors, Chin. J. Chem. Eng. 27 (2) (2019) 314–321, https://doi.org/10.1016/j.cjche.2018.05.006.

[36] L. H. Gaabour, Analysis of spectroscopic, optical and magnetic behaviour of PVDF/PMMA blend embedded by magnetite (Fe3O4) nanoparticles, *Opt. Photonics J.*, 10 (8) (2020) 8, 10.4236/opj.2020.108021.

[37] T. Cai, et al., Ultrafine Ag@AgI nanoparticles on cube single-crystal Ag3PO4 (1 0 0): An all-day-active Z-Scheme photocatalyst for environmental purification, J. Colloid Interface Sci. 533 (2019) 95–105, https://doi.org/10.1016/j.jcis.2018.08.074.

[38] F. Deng, L. Zhao, X. Luo, S. Luo, D.D. Dionysiou, Highly efficient visible-light photocatalytic performance of Ag/AgIn5S8 for degradation of tetracycline hydrochloride and treatment of real pharmaceutical industry wastewater, Chem. Eng. J. 333 (2018) 423–433, https://doi.org/10.1016/j.cej.2017.09.022.

[39] F.Y. Ban, S.R. Majid, N.M. Huang, H.N. Lim, Graphene Oxide and Its Electrochemical Performance, Int. J. Electrochem. Sci. 7 (5) (2012) 4345–4351, https://doi.org/10.1016/S1452-3981(23)19543-5.

[40] K. O-Rak, E. Phakdeepataraphan, N. Bunnak, S. Ummartyotin, M. Sain, H. Manuspiya, Development of bacterial cellulose and poly(vinylidene fluoride) binary blend system: Structure and properties, *Chem. Eng. J.*, 237 (2014) 396–402, 10.1016/j.cej.2013.10.032.

[41] Mahmoud. A. E. Aleem Ali, Ali. El-Remaily, Synthesis of pyranopyrazoles using magnetic Fe3O4 nanoparticles as efficient and reusable catalyst, *Tetrahedron*, 70 (18) (2014) 2971–2975, 10.1016/j.tet.2014.03.024.

[42] N. Meng, et al., Ultrahigh β-phase content poly(vinylidene fluoride) with relaxor-like ferroelectricity for high energy density capacitors, Nat. Commun. 10 (1) (2019) 4535, https://doi.org/10.1038/s41467-019-12391-3.

[43] K. Yang, et al., Graphene oxide nanofiltration membranes containing silver nanoparticles: tuning separation efficiency via nanoparticle size, Nanomaterials 10 (3) (2020) 454, https://doi.org/10.3390/nano10030454.

[44] Y. Zhang, X. Duan, B. Tan, Y. Jiang, Y. Wang, T. Qi, PVDF microfiltration membranes modified with AgNPs/tannic acid for efficient separation of oil and water emulsions, Colloids Surf. Physicochem. Eng. Asp. 644 (2022) 128844, https://doi.org/10.1016/j.colsurfa.2022.128844.

[45] H. Gümüş, Catalytic performance of polyvinylidene fluoride (PVDF) supported TiO2 additive at microwave conditions, *J. Turk. Chem. Soc. Sect. Chem.*, 7(2) (2020) 361–374, 10.18596/jotcsa.610886.

[46] M. Kazemi, M. Jahanshahi, M. Peyravi, Hexavalent chromium removal by multilayer membrane assisted by photocatalytic couple nanoparticle from both permeate and retentate, J. Hazard. Mater. 344 (2018) 12–22, https://doi.org/10.1016/j.jhazmat.2017.09.059.

[47] Y. Yang, et al., Synergistic photocatalytic-photothermal contribution induced by Pd-TiO2/PEDOT immobilized in PVDF membrane for enhanced water purification, Chem. Eng. J. 494 (2024) 153168, https://doi.org/10.1016/j.cej.2024.153168.

[48] H. Gumus, B. Büyükkıdan, A facile preparation of biochar-anchored magnetic photocatalytic PVDF composite for water remediation, Colloid Polym. Sci. 302 (1) (2024) 103–115, https://doi.org/10.1007/s00396-023-05177-z.

[49] F. Zhao, Y. Yang, S. Ji, R. Yu, X. Li, Z. Zhou, Photocatalysis-Fenton mechanism of rGO-enhanced Fe-doped carbon nitride with boosted degradation performance towards rhodamine B, J. Water Process Eng. 55 (2023) 104080, https://doi.org/10.1016/j.jwpe.2023.104080.

[50] T. Li, Z. Cheng, L. Cao, X. Jiang, L. Fan, Interactions of two food colourants with BSA: analysis by *Debye-Hückel* theory, Food Chem. 211 (2016) 198–205, https://doi.org/10.1016/j.foodchem.2016.05.053.

[51] H. Gumus, Infrared responsive PVDF filtration membrane prepared with quince seed extract, *Mendeley Data, V1*, 10.17632/cdwmr87j7c.1.